



Published in final edited form as:

J Instrum. 2021 March ; 16(3): . doi:10.1088/1748-0221/16/03/p03031.

Development of a PET/EPRI combined imaging system for assessing tumor hypoxia

H. Kim^a, B. Epel^{b,c}, S. Sundramoorthy^{b,c}, H.-M. Tsai^a, E. Barth^{b,c}, I. Gertsenshteyn^{a,b,c}, H. Halpern^{b,c}, Y. Hua^d, Q. Xie^e, C.-T. Chen^a, C.-M. Kao^a

^aDepartment of Radiology, University of Chicago, Chicago, IL 60637

^bDepartment of Radiation and Cellular Oncology, University of Chicago, Chicago, IL 60637

^cCenter for EPR Imaging In Vivo Physiology, University of Chicago, Chicago, IL 60637

^dRaycan Technology Co, Ltd., Suzhou, Jiangsu, China

^eHuazhong University of Science and Technology, Biomedical Engineering Department, Wuhan, Hubei, China

Abstract

Precise quantitative delineation of tumor hypoxia is essential in radiation therapy treatment planning to improve the treatment efficacy by targeting hypoxic sub-volumes. We developed a combined imaging system of positron emission tomography (PET) and electron para-magnetic resonance imaging (EPRI) of molecular oxygen to investigate the accuracy of PET imaging in assessing tumor hypoxia. The PET/EPRI combined imaging system aims to use EPRI to precisely measure the oxygen partial pressure in tissues. This will evaluate the validity of PET hypoxic tumor imaging by (near) simultaneously acquired EPRI as ground truth. The combined imaging system was constructed by integrating a small animal PET scanner (inner ring diameter 62 mm and axial field of view 25.6 mm) and an EPRI subsystem (field strength 25 mT and resonant frequency 700 MHz). The compatibility between the PET and EPRI subsystems were tested with both phantom and animal imaging. Hypoxic imaging on a tumor mouse model using ¹⁸F-fluoromisonidazole radio-tracer was conducted with the developed PET/EPRI system. We report the development and initial imaging results obtained from the PET/EPRI combined imaging system.

Keywords

Multi-modality systems; Positron Emission Tomography; Electron-Paramagnetic Resonance Imaging; Tumor Hypoxia

1 Introduction

Because of the rapid proliferation of cancer cells outgrowing blood supply, the amount of oxygen available is limited in some tumor regions distant from blood vessels. Tumor

hypoxia [1, 2] refers to the lower oxygen concentration in tumor tissue, typically below 10 torr, and it is a characteristic feature of human and animal solid tumors. Hypoxia is known to promote tumor progression and migration by changing its metabolism to adapt to oxygen deprived environment [3, 4]. It has been known that hypoxic tumors are more resistant to radiation therapy [5–7], and require additional dose delivery for effective treatment. Therefore, precise delineation of hypoxic tumor region is essential for targeting only hypoxic sub-volume within the tumor in radiation therapy to improve the treatment outcome [8–11].

In the clinic, PET imaging with radio-tracers such as ^{18}F -fluoromisonidazole (F-MISO) [12,13] has been used for hypoxic tumor imaging, which exploits the mechanism of misonidazole binding intracellularly at oxygen-depleted sites 2–4 hours post-injection. However, F-MISO PET imaging has not yet beneficially guided radiation therapy treatment for hypoxic tumors. For example, a recent phase-II clinical study [14] showed that dose painting based on F-MISO PET imaging did not significantly improve the treatment outcomes.

Currently, the F-MISO uptake and binding mechanisms in hypoxic tumor are not clearly understood [15]. Other factors, such as the vascular structure and pH in the micro-environment, have been observed to affect the F-MISO absorption within a hypoxic region [16, 17]. These factors substantially complicate the correlation between the degree of hypoxia and F-MISO uptake. On the other hand, in preclinical studies, the effectiveness of oxygen imaging by electron para-magnetic resonance imaging (EPRI) for targeting hypoxic tumors has been demonstrated [11, 18, 19]. EPRI is a non-invasive imaging technology based on the detection of unpaired electron spins of injectable spin probe subjected to a magnetic field, and is capable of quantitative measurements of the absolute partial pressure of oxygen (pO_2) in tissue [20–22]. However, EPRI is not available for clinical use presently.

We recently initiated a project to investigate the potential of PET imaging in assessing tumor hypoxia in small-animal settings. In the project, we developed a combined small-animal PET and EPRI imaging system to allow simultaneous or rapid succession imaging so that we can use EPR oxygen imaging as a gold standard for in vivo measurement of tissue pO_2 to evaluate the accuracy of PET hypoxia imaging, and to develop correction methods if necessary. The (near) simultaneous PET/EPR operation ensures the recording of the same physiological and biochemical changes in the tissue, and accordingly reflects the correlations between PET and oxygen images more accurately. PET-EPR image registration is not required with the combined system which is not the case for separate PET and EPR scanners.

In this article, we present the development of the combined PET/EPRI system and the initial imaging results obtained by using the system.

2 Material and Methods

2.1 PET subsystem

The PET subsystem was originally developed as an insert for a small animal imaging MRI. It consists of 14 detector modules, which are installed within a cylindrical supporting structure that has a 60 mm inner diameter and a 115 mm outer diameter. Each detector module uses an array of 8×4 LYSO scintillators (each LYSO crystal is 3×3×10 mm³) and two Hamamatsu MPPC arrays (S13361–3050NE or S12642–0404-PA). The scintillators within the array are optically isolated by using enhanced specular reflector (ESR, 3MTM), and are coupled individually to SiPMs (3.2 mm pitch) in the MPPC array. The axial field of view of the PET detector is 25.6 mm. A strip-line based multiplexing method [23] is used for SiPM signal readout. An earlier prototype detector module [23, 24] used 8 SiPMs of 4.0×4.4 mm² active area (SPM42–75, STM) on a strip-line. In comparison, the detector module of the reported system used Hamamatsu MPPC arrays instead due to its smaller pixel size and more uniform gain between SiPM pixels. It also has 16 SiPMs on a strip-line to achieve a higher multiplexing ratio. The 32 SiPM outputs from a detector module are routed to two strip-lines implemented in a strip-line board (SLB), which is a 18×110 mm² printed circuit board. The SLB outputs are connected to a multi-voltage threshold (MVT) waveform sampling board [25] placed away from the MRI magnetic and radio-frequency (RF) fields via 5 m long miniature coaxial cables for signal digitization. The MVT board implements voltage-based sampling of PET signals as following. The board provides 4 user-definable voltage thresholds, which in this study are set to 50, 150, 300 and 600 mV. The leading and trailing transitions of a PET signal over and below these thresholds are obtained by comparators and the transition times are determined by time-to-digital converters (TDC) with 95 ps bin width. The known voltage thresholds and the TDC produced time stamps are packed along with the channel number to a data acquisition computer through an Ethernet interface. The comparators and TDCs are all implemented by using field programmable gate arrays (FPGAs). The performance and MR compatibility of this prototypical PET insert was previously characterized in experiments with a Bruker BioSpec 9.4 T MR scanner (Billerica MA). Figure 1(a) shows a photo of the PET insert. More details on the design and performance characterization of the PET insert are described in our previous publication [26].

2.2 EPRI subsystem

The EPRI subsystem is a 700 (± 20) MHz pulse imager/relaxometer utilizing an inversion recovery electron spin echo (IRESE) acquisition method [22]. It consists of a parallel face 25 mT permanent magnet with a 12 cm gap, 2 mT main field offset coil, three planar orthogonal gradient coils (30 mT/m maximum gradient), an RF resonator and RF control electronics. The resonator is located inside the PET system while the offset coils are placed in between the PET system and the magnet. The RF resonator of the EPRI, shown in Figure 1(b), is a loop-gap resonator in reflection mode for both exciting and detecting RF signals at 700 MHz. The resonator has a cylindrical 19 mm-diameter access that is 15 mm in length. It is embedded in a plastic spacer for positioning at the isocenter of the gradient fields and the PET system. The object to be imaged is placed within the resonator as shown in Figure 1(c). A 4 kW TOMCO RF amplifier is used to power RF pulses, though only 250 W was used for

our experiments. The homodyne bridge scheme and control method similar to [27] is used. The instrument is controlled using SpecMan4EPR software [28].

2.3 Combined system and alignment

Figure 1(c) shows the combined PET/EPRI system encased in a $40 \times 40 \times 31$ cm³ frame. Both the center of the resonator and that of the PET field of view are aligned with the center of the magnets.

Data acquisition and processing of the PET and EPRI subsystems are accomplished separately by two computers. For EPRI, the IRESE imaging sequence was used with 201 projections and a maximum gradient of 7.5 mT/m. Nine time delays between the inversion and the electron spin echo detection were used to measure relaxation times. Image acquisition time was about 7 minutes. The data were reconstructed using a filtered back-projection (FBP) algorithm [29]. PET data were acquired as list-mode data of singles events; post acquisition they were processed to produce coincidence data that were then reconstructed by using a line-of-response based maximum likelihood expectation maximization (MLEM) algorithm [30]. The PET image reconstruction code was previously validated in imaging studies of a ²²Na point source, a ⁶⁸Ge line source, and a custom-made resolution phantom [26].

Alignment between the PET and EPRI system was assessed by imaging a phantom shown in Figure 2(a). The phantom holds 5 capillary tubes; three tubes were filled with ¹⁸F-fluorodeoxyglucose (FDG) for PET, and the other two tubes were filled with 1 mM of trityl spin probe solution [31] for EPRI. Figure 2(b) shows a PET/EPRI combined image of the phantom. The PET image of the 3 FDG-filled capillary tubes is shown in greyscale, and EPRI image of the 2 trityl-filled capillary tubes is shown in color. Figure 2(c) shows an intensity profile of the PET image through the center of the 3 capillary tubes. The PET and EPRI systems were previously evaluated to have an image resolution of approximately 1.6 mm and 1.0 mm, respectively [26]. The intensity profiles (EPRI intensity profiles not shown) indicate that these resolutions are maintained by the combined system.

2.4 Small animal imaging

Small animal imaging followed the protocol approved by the University of Chicago's Institutional Animal Care and Use Committee. Squamous cell carcinoma tumor cells were grown in the leg of a C3H mouse. The animal was positioned into an animal bed which was equipped with a set of 4 non-parallel capillary tubes for registration purpose. The tumor area was secured using polyvinyl siloxane (PVS) dental mold material, as shown in Figures 2(d), and the mold was placed in the resonator hole. F-MISO was used for PET hypoxic imaging.

A bolus of F-MISO was injected intravenously through a tail vein cannula. EPRI acquisition began 1.5 hours post F-MISO injection. During EPRI data acquisition, the trityl spin probe was infused continuously through cannulation at a rate of 240 μ l/h. Two or three 7-minute EPRI images were taken in sequence during which list mode PET data were continuously acquired. This simultaneous imaging session lasted 20–30 minutes. For evaluation, an additional PET-only imaging was conducted beginning 2 hours post F-MISO injection to collect PET data free of the interference of the EPRI pulse sequences.

In addition to PET/EPRI imaging, MR T2-weighted image of the animal was also obtained for anatomical reference. MRI was done separately, after PET/EPRI imaging, by using a preclinical Bruker 9.4 T scanner (Billerica, MA) employing the Rapid Imaging with Refocused Echo (RARE) sequence. The four non-parallel capillary tubes placed around the animal bed were used as fiducial markers for registration of EPR and MR images. Each capillary tube contained 1 mM of trityl spin probe solution that is detectable by both EPRI and MRI.

3 Results

3.1 PET/EPRI mutual interference

Effects on EPRI due to PET was found to be negligible from the comparison of the capillary tube phantom images obtained before and after installation of the PET subsystem. However, the PET subsystem, as the detector modules had no RF shielding, picked-up EPRI RF pulses during simultaneous PET/EPRI imaging. To investigate the effect, we observed the singles count rate and the pulse shape as determined by the MVT samples. Figure 3(a) shows that during RF pulsing the singles count rate increases significantly, due to the detection of spurious events associated with the EPRI RF pulses. However, with MVT data acquisition, these spurious RF events can be effectively rejected by off-line data processing.

As stated above, MVT sampling produces a leading and trailing sample a teach voltage threshold to yield 8 samples for each signal. Figures 3(b) and 3(c) show the signal waveforms estimated from these MVT samples (circles) for a real scintillation pulse and a spurious RF event, respectively. In this work, a simple piecewise linear interpolation-based method is used for estimating signal waveform. The leading portion of the waveform between the 1st and the 4th samples is obtained by linearly interpolating these samples, that before the 1st sample by extrapolating the interpolation line of the 1st and 2nd samples until it reaches zero, and that after the 4th samples by extrapolating the interpolation line between the 3rd and 4th samples until it meets the trailing portion of the waveform, which itself is obtained from the 5th to 8th samples in a similar way. Evidently, the point where the leading and trailing portions meet defines the peak of the waveform. Also shown in Figure 3(b) is the pulse waveform obtained by a bi-exponential fitting for LYSO/MPPC MVT data that was previously proposed and validated in [25]. Although the piecewise linear interpolation-based method was not as accurate, it was much faster to compute and was found to yield adequate energy resolution for the proposed system.

It was observed that the spurious RF events have a shorter duration than the scintillation pulses. The histogram in Figure 3(d) shows that the falling time (calculated as the time difference between the 5th and 8th MVT samples) of the spurious RF events and actual scintillation events have well separated distributions, with the former being approximately 67 ns and the latter approximately 130 ns. Consequently, events having falling time smaller than 95 ns were identified as spurious RF events and rejected before energy qualification and coincidence filtering. Figure 3(e) shows the singles count rate after implementation of this rejection method. Figure 3(f) shows the pulse-height histograms of a detector pixel before and after applying the rejection method on the EPRI-on data. (Note that the y-axis uses

logarithmic scale in Figure 3(f).) The pulse-height of single event was calculated by integrating the area under the interpolated waveform.

To check the effectiveness of the proposed RF-event rejection method, a tumor in the leg of a female mouse was imaged. 4.0 MBq FDG was injected to the female mouse (21.0 gram), and imaging started 35 minutes post-injection. Two PET data sets were obtained for comparison: one data set was collected while EPRI was off (EPRI-off data), and the other set was acquired while EPRI was on but processed by employing the RF-event rejection method (EPRI-on, RF-rejected data). Table 1 summarizes the acquisition time and the resulting numbers of coincidence events. The comparable numbers of coincidence events suggests the effective removal of spurious RF events by the proposed method. Figure 4 shows the PET images obtained from the two data sets, co-registered to the MRI T₂-weighted image for visualization. The PET images obtained from the EPRI-on, RF-rejected data set do not show noticeable artifacts, and are similar to the images from the EPRI-off data. Note that the data sets were acquired at approximately 15 minutes apart; the slight but observable differences between the images possibly reflect temporal physiological changes that occur between the imaging sessions.

3.2 F-MISO and EPRI pO₂: animal imaging

We have conducted 10 mice F-MISO imaging using the PET/EPRI combined system. A typical image is shown in Figure 5 showing a mouse (23.9 gram) with a leg-born SCCVII squamous cell carcinoma immobilized in way similar to that shown in Figure 2(d). An MR T₂ image was acquired for delineating the tumor region as an anatomical reference after PET/EPRI imaging. Figure 5(top) shows the tumor boundary marked on the MR images at three different slices. Figure 5(middle) shows the corresponding PET images. High F-MISO uptake are shown in red and they are observed to appear within the tumor boundary. Figure 5(bottom) shows a pO₂ image by the EPRI for the same image slices. The hypoxic regions within the tumor, defined as pO₂ < 10 torr, is indicated by dark blue color in the image. Some hypoxic regions are overlapped in both F-MISO image and EPRI oxygen images. However, there is also discrepancy between images.

4 Discussion

We have integrated a PET system with an EPRI system and produced successful imaging results for animals. Recently, a combined PET/PERI system was reported by Tseytlin et al. [32], showing successful imaging of a multi-modality phantom containing trityl and FDG solution, but no animal imaging results. This system is different from ours reported here in terms of the PET detector technology and the integration of the PET and EPRI systems. It is a 21 cm inner diameter ring made of 12 detector modules, each of which consists of a 32×32 array 1.5×1.5×10 mm³ LYSO crystals (1.57 mm pixel) coupled to a 10×10 array of 3×3 mm² SiPMs (4.85 mm pitch). Readout of the 10×10 SiPMs is based on the conventional charge division multiplexing to reduce the signals to 2×2, and these signals are acquired by using the conventional analog-to-digital converters (ADC) and TDCs. As its diameter is larger than the gap between the EPRI magnets, the PET ring cannot fit with the EPRI system in the way shown in Figure 1(c). Instead, it “sits” on the bottom EPRI magnet with a 20° tilt

angle to allow some access to the imaging-sensitive volume. Another crucial important difference lies in the design of the EPR oxygen imaging system. The EPR imager of Tseytlin et al. utilizes Rapid Scan (RS) EPR acquisition [33] measuring pO₂ with spin-spin (SS) relaxation based linewidth measurement while we use spin-lattice relaxation (SLR) measured with pulse mode inversion recovery acquisition. SS relaxation based pO₂ measurements are more susceptible to confounding broadening of the spin probe linewidth by the spin probe itself to which SLR is far less susceptible [22]. Thus the proposed system is uniquely suitable to study the effects of hypoxia.

While we reported successful imaging without PET detector shielding, for optimal imaging performance we believe some shielding is still necessary. However, we desire to mitigate the shielding requirement as much as possible to maintain a simple and compact detector design. Recently, we considered a new SLB design to provide inherent shielding of the PET signal traces. The current SLB design shown in Figure 6(a) uses PCB with a single ground plane. In the new SLB, another ground plane is added so that the SiPM signal traces inside the PCB are laid between the two ground planes, as shown in Figure 6(b). A preliminary comparison test between the current and new design SLB was conducted by using single detector module that was coupled to the current or new SLB. The result shows that the EPR RF interference is significantly reduced with the newly designed SLB. Exemplary waveforms of RF noise events, recorded by the DRS4 waveform sampler [34], for the two SLB boards are shown in Figures 6(c) and (d). The amplitude of RF signal appearing on the PET electronics was reduced from often exceeding 700 mV to 50 mV. The percentage of spurious RF events in singles (without the proposed RF rejection method) also is reduced from 76% to 2.6%. We plan to use this new SLB in our next implementation of the PET system. We will also consider the use of thin copper foils to wrap the PET insert for improved shielding.

5 Summary

Precise delineation of hypoxic region in tumor is essential for improving the outcome of oxygen image-guided radiation therapy treatment for hypoxic tumor. PET imaging with F-MISO has been used for hypoxic tumor imaging in clinical trials. However, due to the complexity of F-MISO accumulation and its possible dependence on factors other than hypoxia, F-MISO PET imaging has failed to produce accurate assessment of hypoxic tumor regions *in vivo*. Toward quantitative F-MISO PET imaging, we prototyped a PET/EPRI combined system for small animal imaging for assessing, and potentially calibrating, F-MISO PET hypoxia imaging by using simultaneous EPRI oxygen images as reference. The initial F-MISO and EPR imaging on mouse model hypoxic tumor was successfully conducted using the developed system.

The PET scanner was observed to pick-up RF noises during simultaneous PET/EPRI operation. An effective RF-event rejection method was developed by exploiting the difference between the waveform features of the scintillation and RF events. A newly designed SLB board that can better shield the PET signals from EPRI pulsing is also tested and the result is encouraging. A more comprehensive animal imaging with the developed PET/EPRI system is undergoing and we are in the process of analyzing the correlations

between the resulting F-MISO PET and EPRI oxygen images, and with other physiological parameters derived from MRI imaging, to develop a more complete understanding of F-MISO uptake by healthy and tumor tissues.

Acknowledgments

The authors acknowledge that this work was supported in part by the National Institutes of Health under Grant numbers R01 CA236385, R01 CA098575, R03 EB027343, R01 EB029948, R50 CA211408, P30 CA014599, P41 EB002034, S10 OD025265, and T32 EB002103. We are also grateful for excellent support from Integrated Small Animal Imaging Research Resource and the Cyclotron facility at the University of Chicago.

References

- [1]. Hockel M and Vaupel P, Tumor hypoxia: definitions and current clinical, biologic, and molecular aspects, *J. Natl. Cancer Inst.* 93 (2001) 266. [PubMed: 11181773]
- [2]. Walsh JC, Lebedev A, Aten E, Madsen K, Marciano L and Kolb HC, The clinical importance of assessing tumor hypoxia: relationship of tumor hypoxia to prognosis and therapeutic opportunities, *Antioxid redox signal.* 21 (2014) 1516. [PubMed: 24512032]
- [3]. Sullivan R and Graham CH, Hypoxia-driven selection of the metastatic phenotype, *Cancer Metastasis Rev.* 26 (2007) 319. [PubMed: 17458507]
- [4]. Lu X and Kang Y, Hypoxia and hypoxia-inducible factors: master regulators of metastasis, *Clin. Cancer. Res.* 16 (2010) 5928. [PubMed: 20962028]
- [5]. Gray LH, Conger AD, Ebert M, Hornsey S and Scott OC, The concentration of oxygen dissolved in tissues at the time of irradiation as a factor in radiotherapy, *Br. J. Radiol.* 26 (1953) 638. [PubMed: 13106296]
- [6]. Brizel DM, Dodge RK, Clough RW and Dewhirst MW, Oxygenation of head and neck cancer: changes during radiotherapy and impact on treatment outcome, *Radiother. Oncol.* 53 (1999) 113. [PubMed: 10665787]
- [7]. Moeller BJ, Richardson RA and Dewhirst MW, Hypoxia and radiotherapy: opportunities for improved outcomes in cancer treatment, *Cancer Metastasis Rev.* 26 (2007) 241. [PubMed: 17440683]
- [8]. Rajendran JG, Hendrickson KRG, Spence AM, Muzi M, Krohn KA and Mankoff DA, Hypoxia imaging-directed radiation treatment planning, *Eur. J. Nucl. Med. Mol Imaging* 33 (2006) 44. [PubMed: 16763816]
- [9]. Thorwarth D, Eschmann SM, Paulsen F and Albert M, Hypoxia imaging-directed radiation treatment planning, *Int. J. Radat. Oncol. Biol. Phys.* 68 (2007) 291.
- [10]. Lee CT, Boss MK and Dewhirst MW, Imaging tumor hypoxia to advance radiation oncology, *Antioxid redox signal.* 21 (2014) 313. [PubMed: 24329000]
- [11]. Epel B, Maggio MC, Barth ED, Miller RC, Pelizzari CA, Krzykawska-Serda M et al., Oxygen-guided radiation therapy, *Int. J. Radiation Oncol. Biol. Phys.* 103 (2019) 977.
- [12]. Rasey JS, Grunbaum Z, Magee S, Nelson NJ, Olive PL, Durand RE et al., Characterization of radiolabeled fluoromisonidazole as a probe for hypoxic cells, *Radiat. Res.* 111 (1987) 292. [PubMed: 3628717]
- [13]. Rajendran JG and Krohn KA, F18 fluoromisonidazole for imaging tumor hypoxia: imaging the microenvironment for personalized cancer therapy, *Semin. Nucl. Med.* 45 (2015) 151. [PubMed: 25704387]
- [14]. Vera P, Thureau S, Chaumet-Riffaud P, Modzelewski R, Bohn P, Vermandel M et al., Phase ii study of a radiotherapy total dose increase in hypoxic lesions identified by 18f-misonidazole pet/ct in patients with non-small cell lung carcinoma (rtep5 study), *J. Nucl. Med.* 58 (2017) 1045. [PubMed: 28254869]
- [15]. Masaki Y, Shimizu Y, Yoshioka T, Tanaka Y, Nishijima K, Zhao S et al., The accumulation mechanism of the hypoxia imaging probe “fmiso” by imaging mass spectrometry: possible involvement of low-molecular metabolites, *Scientific Reports* 5 (2015) 1.

- [16]. Monnich D, Troost E, Kaanders J, Oyen W, Alber M and Thorwarth D, Modelling and simulation of [18f]fluoromisonidazole dynamics based on histology-derived microvessel maps, *Phys. Med. Biol.* 56 (2011) 2045. [PubMed: 21386142]
- [17]. Kipp BH, Faraj C, Li G and Njus D, Imidazole facilitates electron transfer from organic reductants, *Bioelectrochemistry* 64 (2004) 7. [PubMed: 15219240]
- [18]. Elas M, Magwood JM, Butler B, Li C, Wardak R, DeVries R et al., Epr oxygen images predict tumor control by a 50% tumor control radiation dose, *Cancer Res.* 73 (2013) 5328. [PubMed: 23861469]
- [19]. Epel B, Krzykawska-Serda M, Tormyshev V, Maggio MC, Barth ED, Pelizzari CA et al., Spin lattice relaxation epr po₂ images may direct the location of radiation tumor boosts to enhance tumor cure, *Cell Biochem. Biophys.* 75 (2017) 295. [PubMed: 28986856]
- [20]. Berliner JL and Fujii H, Magnetic resonance imaging of biological specimens by electron paramagnetic resonance of nitroxide spin labels, *Science* 227 (1985) 517. [PubMed: 2981437]
- [21]. Halpern HJ, Spencer DP and van Polen J, Imaging radio frequency electron-spin-resonance spectrometer with high resolution and sensitivity for in vivo measurements, *Rev. Sci. Instrum.* 60 (1989) 1040.
- [22]. Epel B, Bowman MK, Mailer C and Halpern HJ, Absolute oxygen r_{1e} imaging in vivo with pulse electron paramagnetic resonance, *Magn. Reson. Med.* 72 (2014) 362. [PubMed: 24006331]
- [23]. Kim H, Chen C-T, Eclov N, Ronzhin A, Murat P, Ramberg E et al., A feasibility study of a pet/mri insert detector using strip-line and waveform sampling data acquisition, *Nucl. Instrum. Methods Phys. Res. A* 784 (2015) 557. [PubMed: 25937685]
- [24]. Kim H, Chen C-T, Eclov N, Ronzhin A, Murat P, Ramberg E et al., A silicon photo-multiplier signal readout using strip-line and waveform sampling for positron emission tomography, *Nucl. Instrum. Methods Phys. Res. A* 830 (2016) 119. [PubMed: 27746514]
- [25]. Xi D, Kao CM, Liu W, Zeng C, Liu X and Xie Q, Fpga-only mvt digitizer for tof pet, *IEEE Trans. Nucl. Sci.* 60 (2013) 3253.
- [26]. Kim H, Hua Y, Chen H-T, Tsai H-M, Chen C-T, Karczmar G et al., Design, evaluation and initial imaging results of a pet insert based on strip-line readout for simultaneous pet/mri, *Nucl. Instrum. Methods Phys. Res. A* 959 (2020) 163575.
- [27]. Epel B, Sundramoorthy SV, Mailer C and Halpern HJ, A versatile high speed 250-mhz pulse imager for biomedical applications, *Concepts Magn. Reson. B* 33 (2008) 163.
- [28]. Epel B, Gromov I, Stoll S, Schweiger A and Goldfarb D, Spectrometer manager: a versatile control software for pulse epr spectrometers, *Concepts Magn. Reson. B* 26 (2005) 36.
- [29]. Anh KH and Halpern HJ, Spatially uniform sampling in 4-d epr spectral-spatial imaging, *J. Magn. Reson.* 185 (2007) 152. [PubMed: 17197215]
- [30]. Shepp L and Vardi Y, Maximum likelihood reconstruction for emission tomography, *IEEE Trans. Med. Imaging* 1 (1982) 113. [PubMed: 18238264]
- [31]. Kuzhelev AA, Trukhin DV, Krumkacheva OA, Strizhakov RK, Rogozhnikova OY, Troitskaya TI et al., Room-temperature electron spin relaxation of triarylmethyl radicals at the x- and q-bands, *J. Phys. Chem. B* 119 (2015) 13630. [PubMed: 26001103]
- [32]. Tseytlin M, Stolin AV, Guggilapu P, Bobko AA, Khramtsov VV, Tseytlin O et al., A combined positron emission tomography (pet)-electron paramagnetic resonance imaging (epri) system: initial evaluation of a prototype scanner, *Phys. Med. Biol.* 63 (2018) 105010.
- [33]. Joshi JP, Ballard JR, Rinard GA, Quine RW, Eaton SS and Eaton GR, Rapid-scan epr with triangular scans and fourier deconvolution to recover the slow-scan spectrum, *J. Magn. Reson.* 175 (2005) 44. [PubMed: 15949747]
- [34]. Ritt S, Dinapoli R and Hartmann U, Application of the drs chip for fast waveform digitizing, *Nucl. Instrum. Methods Phys. Res. A* 623 (2010) 486.

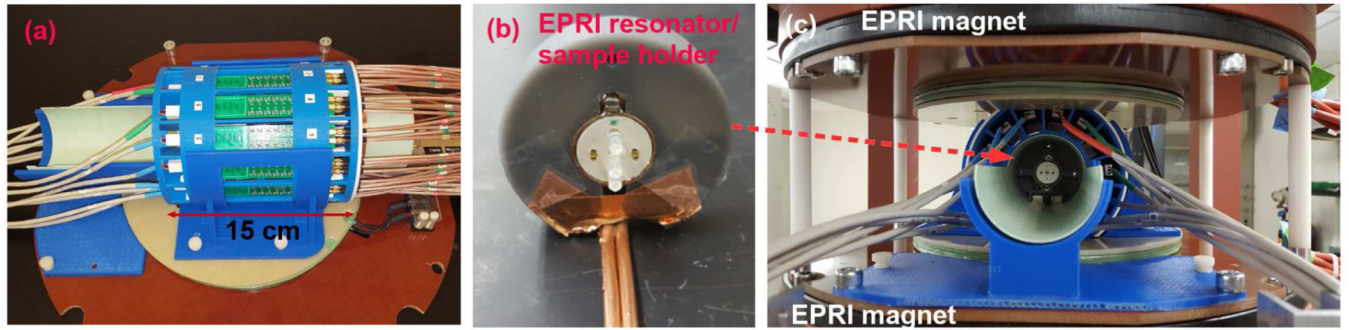


Figure 1.

(a) The PET detector before integration. (b) A loop-gap type EPRI RF resonator. A phantom with capillary tubes is positioned at the center of the resonator for imaging. (c) A PET/EPRI combined system. The PET detector is installed between two permanent EPRI magnets.

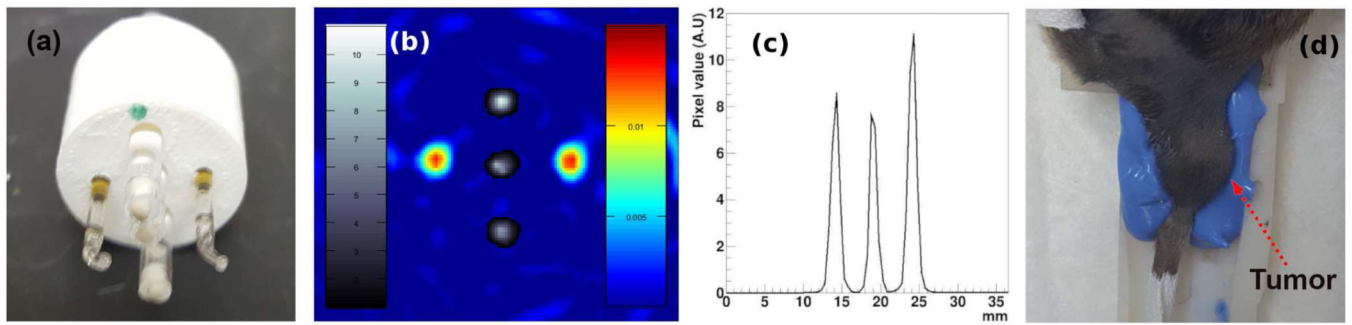


Figure 2.

(a) An imaging phantom with 3 capillary tubes filled with FDG and 2 tubes filled with trityl spin probe solution. (b) A PET/EPRI registered image of the imaging phantom. (c) A profile of the PET image on the line through the centers of the 3 capillary tubes filled with FDG. (d) A tumor-borne mouse leg is immobilized in the animal bed using polyvinyl siloxane mold cast; the bed is placed in the resonator for imaging.

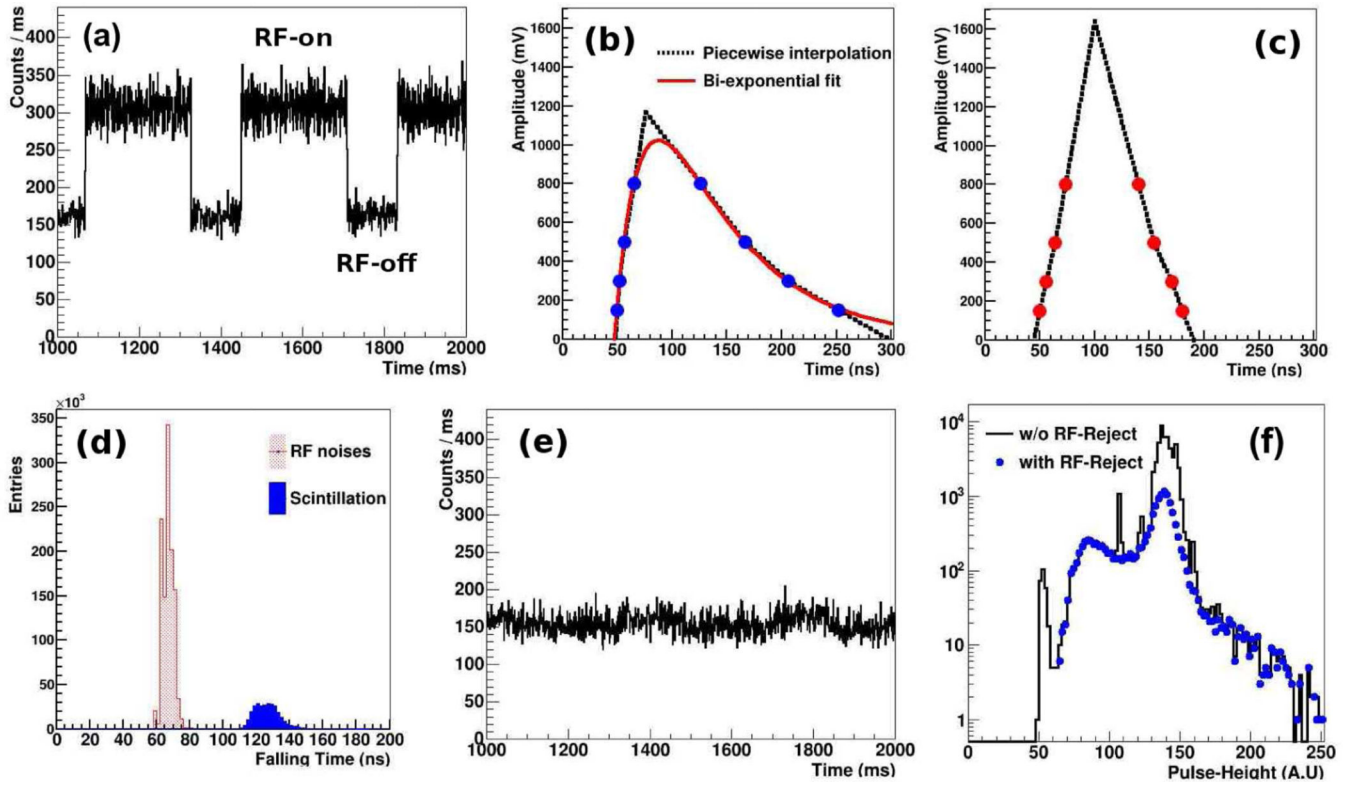


Figure 3.

(a) PET singles event rate as the EPRI RF pulsing is turned on and off. Horizontal axis represents singles event time-stamp recorded in the MVT board. (b) A typical scintillation event consisting of 8 MVT samples (blue circles) and the signal waveforms estimated from them by using a simple piecwise linear interpolation-based method (dashed-line curve) and a bi-exponential fitting function (solid-line curve). (c) The waveform of an exemplary spurious RF event picked up by PET data acquisition. (d) Histogram of the falling time measured from the data acquired during EPRI RF pulsing. (e) Singles event rate after applying the RF rejection. (f) Pulse-height histograms for a detector pixel before and after applying the RF rejection.

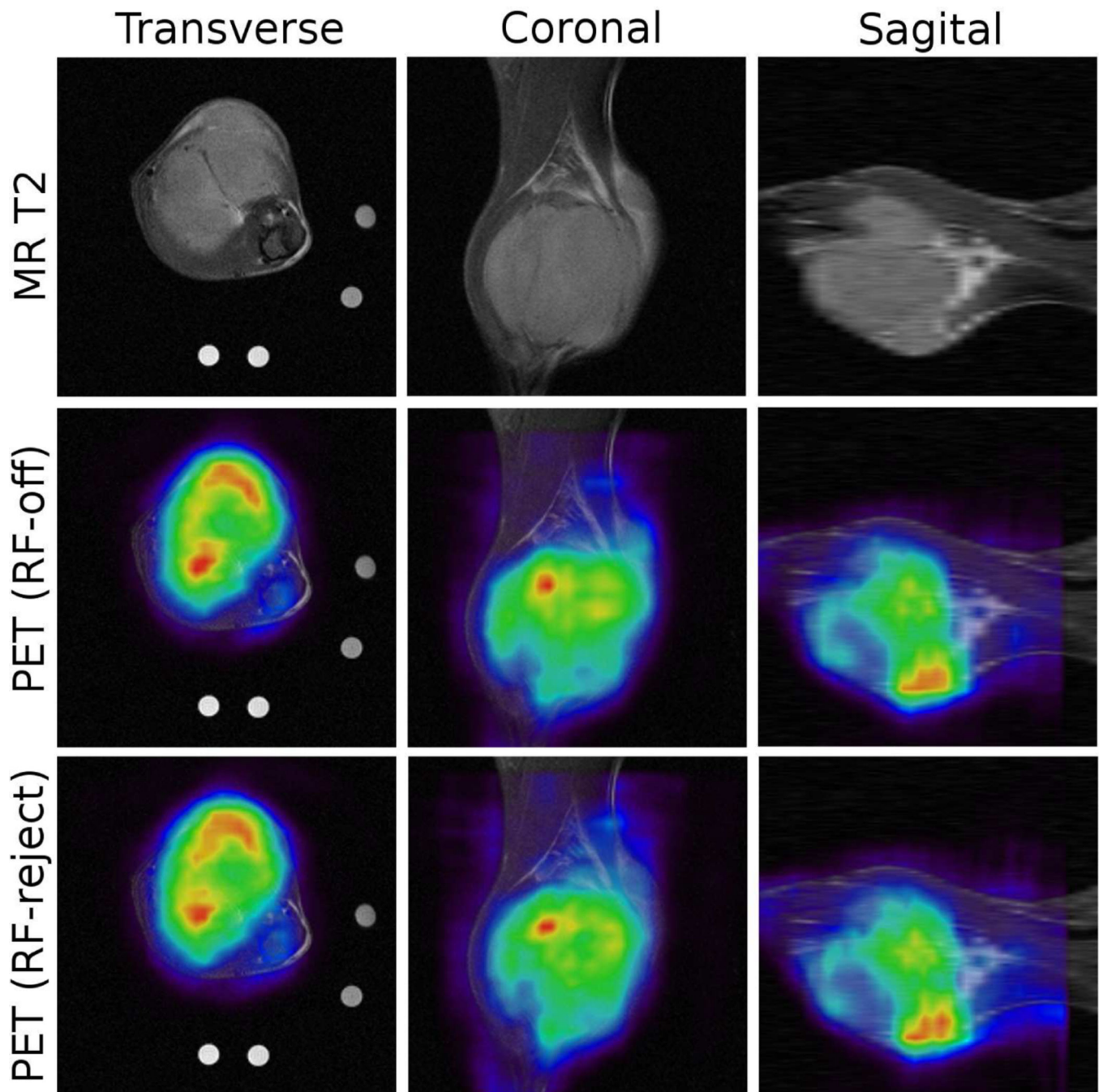


Figure 4.

(top) A MR T2-weighted image of the tumor in a mouse are acquired for anatomical reference. (middle) PET image obtained from the EPRI-off data are registered to the MR image. (bottom) PET image for the same slice obtained from the EPRI-on and RF-rejected data.

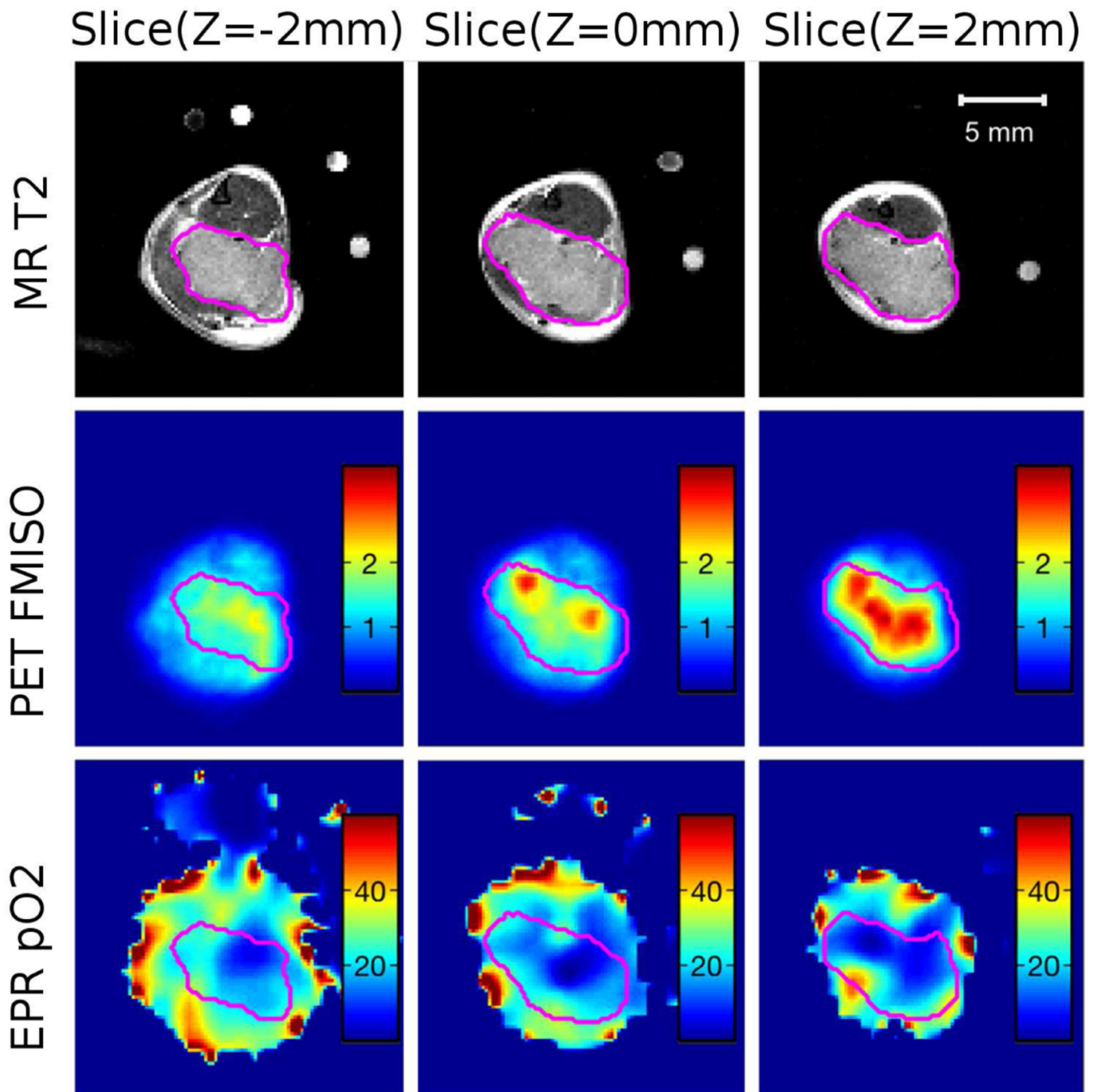


Figure 5.

(top) A MR T₂ image of the tumor in a mouse. The tumor boundary is determined based on the MR image and marked by pink color line. (middle) A PET image for the same slice shows high F-MISO uptake in the tumor. (bottom) pO₂ image acquired by the EPRI. The hypoxic region within the tumor is indicated by dark blue color.

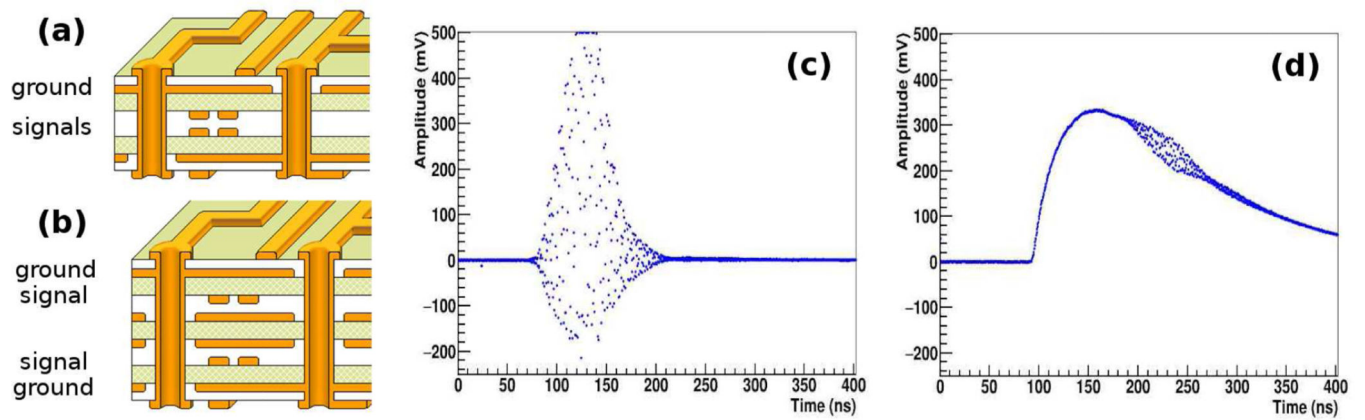


Figure 6.

(a) The PCB layout of strip-line board currently used in the PET (b) The PCB layout in a newly designed strip-line board. (c) An exemplary waveform of RF noise using the current PCB. (d) An exemplary waveform of RF noise using the new PCB. The RF noise is riding on top of scintillation signal.

Table 1.

Comparison of the data acquisition time and the number of coincidence event from the two data sets.

Data set	EPR On	EPR On, RF-rejected	EPR Off
DAQ time (minutes)	15.5	15.5	14.5
Coincidence events	17.4 M	0.71 M	0.68 M

Author Manuscript

Author Manuscript

Author Manuscript

Author Manuscript